

Field-Free Switching of a Spin-Orbit-Torque Device Through Interlayer-Coupling-Induced Domain Walls

Xiaotian Zhao,¹ Lianze Ji,² Wei Liu,^{1,*} Shangkun Li,¹ Long Liu¹,¹ Yuhang Song,¹ Yang Li,¹ Jun Ma,¹ Xingdan Sun,¹ Hanwen Wang,¹ Xinguo Zhao,¹ and Zhidong Zhang¹

¹Shenyang National Laboratory for Materials Science, Institute of Metal Research, Chinese Academy of Sciences, Shenyang 110016, China

²Key Laboratory for Anisotropy and Texture of Materials (MOE), School of Materials Science and Engineering, Northeastern University, Shenyang 110819, China



(Received 27 August 2019; revised manuscript received 26 March 2020; accepted 6 April 2020; published 28 April 2020; corrected 26 August 2020)

The spin-orbit-torque (SOT) device is a promising candidate for the next-generation magnetic random-access memory; however, the static in-plane field needed to induce deterministic switching is a main obstacle for its application in circuits. In this work, we employ the exchange coupling between the Co/Ni/Co trilayer and Tb/Co multilayers in a device to form the domain wall (DW), by whose current-driven propagation the field-free magnetization switching is achieved. The SOT efficiency of the device is highly dependent on the chirality of the Néel-type DW. Meanwhile, the coexistence of two switching modes results in an asymmetric switching phase diagram. We find the competition between the uniform external field and the Dzyaloshinskii–Moriya interaction induces negative feedback to the pinning effect, resulting in a sharp switching process and straight DW profile. Finally, a synthetic antiferromagnetic device is investigated by experiment and micromagnetic simulation to verify the feasibility of using this proposal as the free layer of a magnetic tunneling junction.

DOI: 10.1103/PhysRevApplied.13.044074

I. INTRODUCTION

Manipulating the magnetization by the spin-orbit torque (SOT) in heavy-metal/ferromagnet (HM/FM) systems is a promising mechanism for magnetic random-access memory (MRAM) application [1–3]. The accumulation of polarized spins at the HM/FM interface originated from the spin-Hall effect (SHE) generates Slonczewski-like torque, which enables magnetization switching by in-plane current in a three-terminal device. Compared to two-terminal device, in SOT MRAM, the risk of breakdown through the MgO tunnel layer is eliminated. Moreover, the switching efficiency of a SOT MRAM can be further enhanced by increasing the spin Hall angle [4,5] and the interface transparency [6–10]. These potentials make SOT very promising for next-generation magnetic memory.

However, the requirement of a static in-plane field hinders SOT MRAM from being practicable, since the external field is not applicable in integrated circuits. This problem was first issued by a macro-spin model [2], which shows that the SOT does not favor a certain magnetization direction without the aid of the static in-plane field parallel to the current direction. Further investigation emphasized more on the Dzyaloshinskii–Moriya interaction (DMI)

which universally exists at HM/FM interfaces with large spin-orbit coupling [11]. DMI favors a homochiral Néel-type domain wall (DW), which makes the SOT generate a zero net driving force for the expansion of an enclosed domain nucleation center. An in-plane field applied parallel to the current direction can help break the chirality and make the expansion possible. The minimum in-plane field needed is calculated to be around 10%–25% of the effective DMI field (H_{DM}) in a Pt/Co/MgO system [12]. An intuitive solution to this problem is replacing the external field by an effective field. Different forms of effective fields such as exchange bias [13–15], noncollinear interlayer exchange coupling (IEC) [16–18], gradient magnetic anisotropy [19,20], Rashba field [21], or spin-transfer torque [22] have been employed to replace the in-plane field.

Alternatively, the motion of the homochiral Néel-type DW driven by current-generated SOT can be utilized to achieve the deterministic switching of magnetization in a way similar to the racetrack devices [23–25]. The core issue of this idea is how to get reliable DW sources for both magnetization directions. Using stray field induced by additional magnetic components [26] or DW pinning by geometry effect [27,28] can fix the magnetization in opposite directions at the two ends of the current channel and results in a stable DW. However, these solutions are either

*wliu@imr.ac.cn

too complex for manufacture or hard to realize when the device size shrinks to tens of nanometers.

In this work, we studied field-free magnetization switching assisted by interlayer-coupling induced DW. Based on our previous work [29], a Ru/Pt bilayer is employed to connect Tb/Co pinning layers and a Co/Ni/Co trilayer by Ruderman-Kittel-Kasuya-Yosida (RKKY) coupling. Deterministic current-driven switching is achieved once the magnetizations of the Tb/Co pinning layers are set by the field. The strong RKKY coupling makes it possible to investigate the switching mechanism under competition between the DMI and the external field. Finally, a synthetic antiferromagnet (SAF) structure is fabricated to prove the possibility of achieving magnetic tunneling junction (MTJ) in this design. The geometry-independent nature and compatibility with manufacture make this device design promising in practical and future spintronic research.

II. EXPERIMENTAL DETAILS

The structure and main fabrication procedure of the device are shown in Fig. 1(a). Stacks of Ta(2)/Pt(4)/Co(0.3)/Ni(0.6)/Co(0.3)/Ru(0.7)/Pt(0.3) (thicknesses given in nm) are deposited on a thermally oxidized Si(001) substrate by dc magnetron sputtering under a base vacuum lower than 4.0×10^{-7} Torr. A silica layer thickness of 50 nm is chosen to avoid unwanted domain nucleation induced by Joule heating of the current [30]. The inert Ru/Pt capping layer with total thickness of

1 nm is employed to prevent oxidization of the Co/Ni/Co trilayer. For the FM layer deposited in the subsequent procedure, the 0.7-nm-thick Ru ensures antiferromagnetic (AFM) RKKY coupling [31] with the Co/Ni/Co trilayer, and the 0.3-nm-thick Pt enhances the perpendicular magnetic anisotropy (PMA) [32,33]. During the deposition, the Ar pressure is 2 mTorr and all the deposition rates are among 0.02 to 0.04 nm s⁻¹. Measurement on a superconducting quantum interference device (SQUID) magnetometer shows that the Co/Ni/Co trilayer has a saturation magnetization (M_s) of 750 kA m⁻¹ and an effective out-of-plane anisotropy field $\mu_0 H_{k\text{eff}} = 890$ mT. To form the patterns, standard ultraviolet lithography technology is employed. The first pinning layer (Pad1) has the configuration Co(0.8)/[Tb(1)/Co(0.7)]₈/Ru(2)/Au(10) and the second pinning layer (Pad2) has the configuration Co(0.8)/[Tb(0.7)/Co(0.7)]₈/Ru(2)/Au(10). The purpose of the thick gold layer is to induce a current large enough to keep the magnetization of the coupled areas stable, and 2 nm of Ru is inserted between the TbCo multilayer and the Au layer to isolate possible SOT generated by the Au. The sample is cleaned by rf oxygen plasma for 20 s after development of the photoresist to ensure good contact between the Pt and Co for RKKY coupling. Finally, the stack is patterned by Ar ion etching into the Hall bar with a 10-μm-wide current channel and a Ti(10)/Au(100) electric pad is deposited on the Hall bar [see Fig. 1(b)]. On the same chip, Hall bars without the pinning layers are also made as the reference devices.

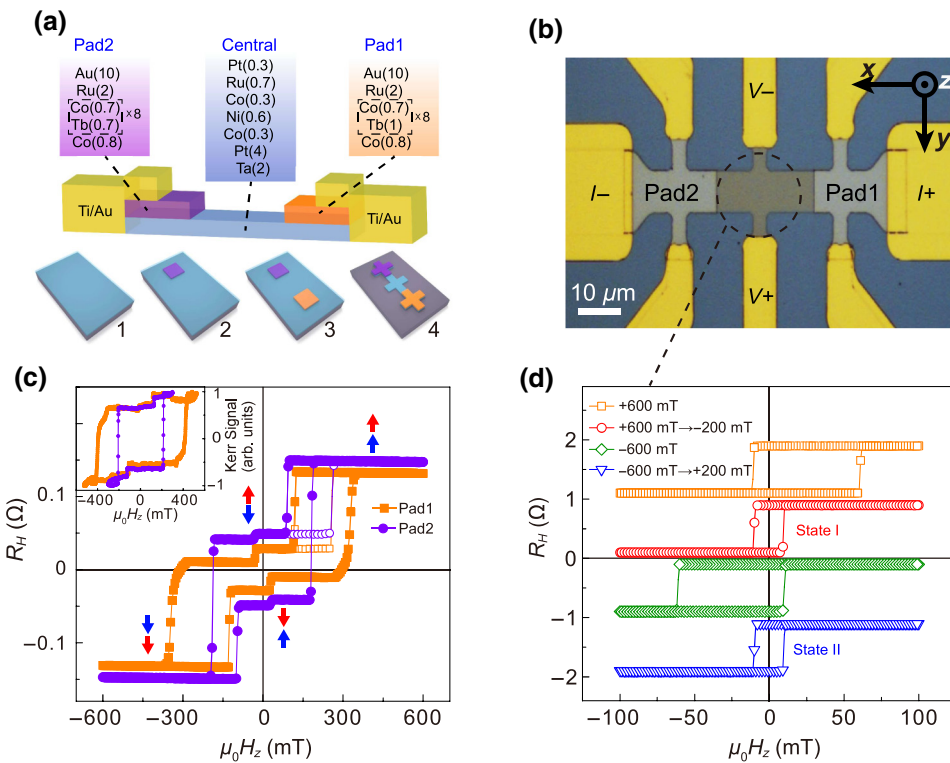


FIG. 1. Structure and magnetic properties of the device. (a) Structure, composition, and the processing procedure of the device: 1, deposition of the expanding central stack; 2 and 3, deposition of the two pads by lift-off method; 4, patterning of the Hall bar by Ar⁺ ion etching (thickness in nm). (b) Photography and transportation measuring configuration of the device. (c) R_H vs H_z loops of Pad1 (orange squares) and Pad2 (purple circles). The arrows indicate the magnetization configuration at different stages (red for net magnetization of Tb/Co and blue for that of Co/Ni/Co). The open symbols show the minor loops of the exchange-coupled Co/Ni/Co trilayer. The inset shows the corresponding MOKE signals. (d) R_H vs H_z loops measured at the central cross after different configurations of setting field. Loops are staggered along the z axis.

The electric current is injected into the main channel of the device by an Agilent 32 200 signal generator through a 10 MHz bandwidth bipolar amplifier. A sinusoidal current of 0.2 mA is applied and the differential anomalous Hall resistance R_H of the device is measured using a Stanford SR830 Lock-in amplifier. The current-driven switching loops are achieved by switching the current to pulses (I_p) with a duration of 1 ms. A home-made magneto-optical Kerr (MOKE) microscope illuminated by a 532-nm light-emitting diode is employed to characterize the domain distribution. The loop-shift method is applied to evaluate the SOT effective field [34]. All measurements and applied-field directions follow the geometry noted in Fig. 1(b).

III. RESULTS AND DISCUSSION

A. Initialization of the magnetization

The R_H values obtained from Pad1 and Pad2 versus H_z are shown in Fig. 1(c). Both sets of loops exhibit sharp signal reversals in the first and third quadrants, which is a typical feature of antiferromagnetic RKKY coupling. The small R_H steps found in the central part of the R_H - H_z loops come from the switching of the magnetization of the central cross of the Hall bar. To distinguish the signal of the Co/Ni/Co trilayer from that of the Tb/Co multilayers, MOKE measurements are carried out, as shown in the inset of Fig. 1(c). Since the MOKE signal is highly sensitive to the depth of the magnetic layer, it is clear that the relatively weakened signals originate from the Co/Ni/Co trilayer, which is covered by the Tb/Co multilayers. The minor loops of the Co/Ni/Co trilayer show an exchange field of $\mu_0 H_{\text{ex}} = 190$ mT for Pad1 and 176 mT for Pad2, corresponding to RKKY coupling $A_{\text{Ru}} = 1.71$ and 1.58 mJ m^{-2} , respectively. The magnetization configurations at different stages of the loops are indicated by the arrows shown in Fig. 1(c). The reversal sequence is attributed to the large out-of-plane anisotropy and partly compensated magnetization of the Tb/Co multilayers. Since the Tb/Co multilayers used here are Co rich, the larger Tb ratio of Pad1 makes its coercivity larger than that of Pad2. Notably, if the multilayer is Tb rich, the coupling between the Co/Tb multilayers and Co/Ni/Co trilayer will be FM like since the RKKY coupling is dominated by $3d$ electrons of transitional FM metal rather than the more localized $4f$ electrons of rare-earth elements (see Note 1 within the Supplemental Material) [35,36].

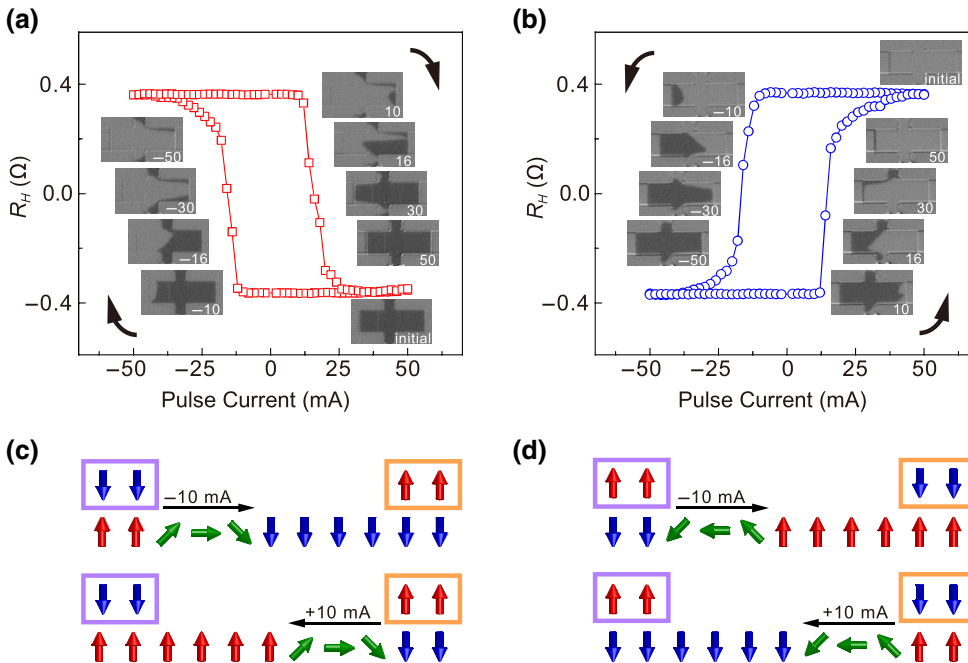
The different coercivities of the two pads offer a window for manipulating the remanence states of the Co/Ni/Co trilayer in the two coupled areas by different configurations of setting field. R_H - $\mu_0 H_z$ loops of the central cross acquired for four different configurations of setting field are represented in Fig. 1(d). The loops measured after a single setting field of $\mu_0 H_z = \pm 600$ mT show obvious biased behavior corresponding to the polarity of the setting field. This bias can be eliminated by adding a setting field of

$|\mu_0 H_z| = 200$ mT that is opposite to the initial setting field of 600 mT. The amplitude of the second setting field is between the coercivity of the two pads, arranging the magnetization of the two pads into opposite directions. The creation and elimination of the biases imply that the coupled Co/Ni/Co trilayer helps the magnetization switching in the central cross by offering DW motion which usually has a lower energy barrier than the domain nucleation. Hereafter, the remanence state after +600 mT and -200 mT setting field is called “State I,” while that after -600 mT and +200 mT magnetization is called “State II.”

B. Field-free switching

Figures 2(a) and 2(b) show the current-driven magnetization switching in the absence of an external field. For both states, the distance between two R_H values at $I_p = 0$ is the same as the one shown in Fig. 1(d), making it credible that the magnetization of the central cross is fully switched during the current-driven process. Based on resistance measurements on a sample with a wedged Pt layer, it is estimated that 76% of the total current is channeled through the Pt layer, and thus the average critical current (I_{cri}) of 15.7 mA corresponds to a current density of $2.98 \times 10^{11} \text{ A m}^{-2}$. Differential MOKE images are attached to the loops to show the domain structure during the current-driven switching sequence. In the case of State I, as shown in Fig. 2(a), the reversal domain appears at the boundary of Pad2 at $I_p = 10$ mA. During the expansion of the reversal domain, the DW shows a curved profile with a central peak, implying that a strong pinning effect exists in the device, especially at the edges of the current channel. This pinning effect will be discussed in detail in Sec. III E. Changing the configuration of the setting field to State II, as shown in Fig. 2(b), the magnetization can still be switched at the same amplitude of I_{cri} while the switching polarity is opposite. The domain always expands from the coupled area with the corresponding magnetization direction, soundly indicating that the pads are the source of the reversal domain.

As depicted by the schematic illustrations in Figs. 2(c) and 2(d), the coupled areas guarantee an up-down ($\uparrow\downarrow$) DW at State I or down-up ($\downarrow\uparrow$) DW at State II. The key to determine the switching polarity is the in-plane component \mathbf{m}_{DW} of the Néel-type DW, which is stabilized by DMI in this case. Considering that the direction of SHE induced SOT is determined by $\mathbf{m} \times (\boldsymbol{\sigma} \times \mathbf{m})$ [2,25], where \mathbf{m} is the magnetic moment and $\boldsymbol{\sigma}$ the spin accumulation along the y axis generated by the SHE, the direction of \mathbf{m}_{DW} can be determined to be \rightarrow at State I and \leftarrow at State II, indicating an anti-clock chirality. This is consistent with the reported chirality of the Co/Ni/Co trilayer [24,37] with Pt underlayer. Since this switching mode depends on the DW motion, we call it “DW motion mode,” and we will call the traditional switching with aid of



$\mu_0 H_x$ “nucleation-expansion mode” in order to distinguish between them.

C. Behaviors under field I: SOT efficiency measurement

To investigate the different behavior of the two switching modes, we measure the effective field generated by the SOT-induced loop-shift method for both the DW-assisted device and the reference Hall bar [34,38,39]. In this method, collinear static magnetic field $\mu_0 H_x$ and bias current (I_b) are applied to the Hall bar during the measurement of R_H versus scanning $\mu_0 H_z$. The expansion of the reversal domain is assisted or suppressed by the SOT, depending on the related directions of I_b , $\mu_0 H_x$, and $\mu_0 H_z$, resulting in a loop shift which represents the effective

FIG. 2. Field-free switching assisted by DWs. (a),(b) Field-free current-driven switching R_H vs I_p loop measured in State I (a) and State II (b) with MOKE images taken for the labeled current. (c), (d) Schematic illustrations of the moment configuration of the Co/Ni/Co trilayer in State I (c) and State II (d) at the moments that the DWs tend to move along with the current direction labeled by black arrows. The different colors represent up (red), down (blue), and chiral rotation (green) of magnetic moment. The hollow rectangles contain net magnetization of the Pad1 (purple) and Pad2 (orange).

field of the Slonczewski-like torque ($\mu_0 H_{SL}$). The slope of linear fitting derived from the relationship between the current densities and the loop shifts represents the conversion efficiency χ from the electric current to SOT effective field. Because of the large coercivity of the Tb/Co ferrimagnet and the strong shunting effect of the highly conductive capping layer [18], the measurement of loop shift is carried out for the DW-assisted device without the risk of erasing the DW.

Since the field-free switching is achieved, it is not odd to see loops of the DW-assisted device shifted by direct current at zero field as shown in Fig. 3(a). The shift directions conform to the loop polarity shown in Fig. 2(a) and the amplitude of the shifts corresponds to the effective field generated by the direct current. The $\chi-\mu_0 H_x$ curves

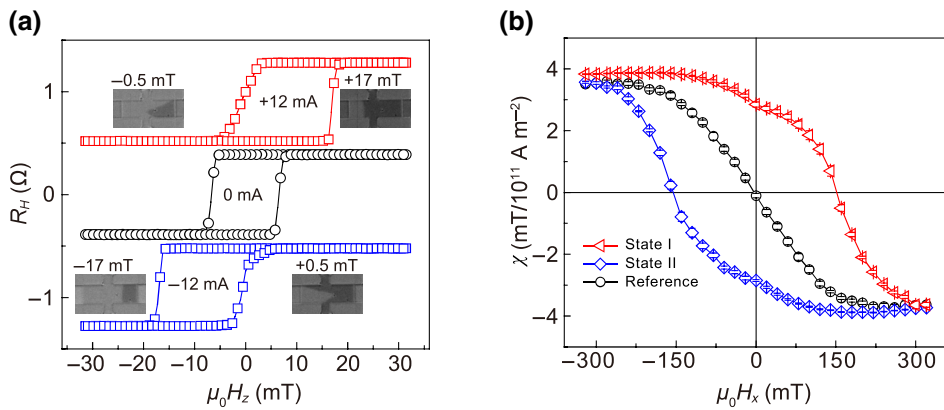


FIG. 3. SOT efficiency measured by the loop-shift method. (a) R_H vs H_z loops of the central area measured at zero field in State I with different bias currents. MOKE images indicate the DW profile during the switching process. Loops are staggered along the z-axis. (b) $\chi-H_x$ curves of the DW-assisted device measured at State I (blue diamonds), State II (red triangles), and the $\chi-\mu_0 H_x$ of the reference device (black circles). The error bars refer to the standard deviation of linear fitting of χ .

of both the DW-assisted device and the reference Hall bar are presented in Fig. 3(b). For the DW-assisted device, two states show opposite χ values at $\mu_0 H_x = 0$ mT. Around ± 300 mT, all three curves saturate at a $|\chi|$ value of $3.6 \text{ mT}/10^{11} \text{ A m}^{-2}$. From the $|\chi|$ value an effective spin-Hall angle $\xi_{\text{SH}} = 0.1$ can be deduced by the relationship [40] $\mu_0 H_{\text{SL}} = \hbar \xi_{\text{SH}} |j_c| / (2|e|M_s t)$, where \hbar is the reduced Planck constant, j_c the charge current density, e the electron charge, M_s the saturated magnetization, and t the thickness of the FM layer. This value is comparable to the value 0.15 reported in the previous work [34] and 0.2 measured by the 1f-2f harmonic method (see Note 2 within the Supplemental Material) [35,41,42]. The same conversion efficiency reflects that the loop shift of the two devices has the same dependence on the DW-driven force induced by SOT.

The biggest differences between these three curves are their different crossing points on the $\mu_0 H_x$ axis, which indicate vanishing SOT efficiency. For the reference Hall bar, the crossing point is positioned very close to the original point. For the two states of the DW-assisted device, the crossing points are positioned on opposite sides of the

$\mu_0 H_x$ axis, with the same distance of $|\mu_0 H_x| = 154$ mT away from the original point. Notably, the $\chi - \mu_0 H_x$ curve of the reference Hall bar also saturates around this value. The saturation of a conventional $\chi - \mu_0 H_x$ curve implies that the chirality of an enclosed domain wall is destroyed by the external field. Hence, this coincidence means that the assisted-DW loses its driving force from SOT when the effective field of DMI ($\mu_0 H_{\text{DM}}$) is fully compensated by $\mu_0 H_x$. Based on this result, the DMI strength $|D|$ can be calculated by using $|D| = \mu_0 M_s H_{\text{DM}} \sqrt{A/K_{\text{eff}}}$ [43], where A is the exchange constant assumed to be 10 pJ m^{-1} , and K_{eff} the effective PMA energy density obtained by SQUID measurement. $|D|$ is calculated to be 0.63 mJ m^{-2} .

D. Behaviors under field II: switching phase diagram

Although the nucleation-expansion mode does not contribute to the $\chi - \mu_0 H_x$ curve of the DW-assisted device because of the large coercivity depicted in Fig. 1(d), its influence exists in the current-driven switching under the static in-plane field. The direct proof of this claim is the

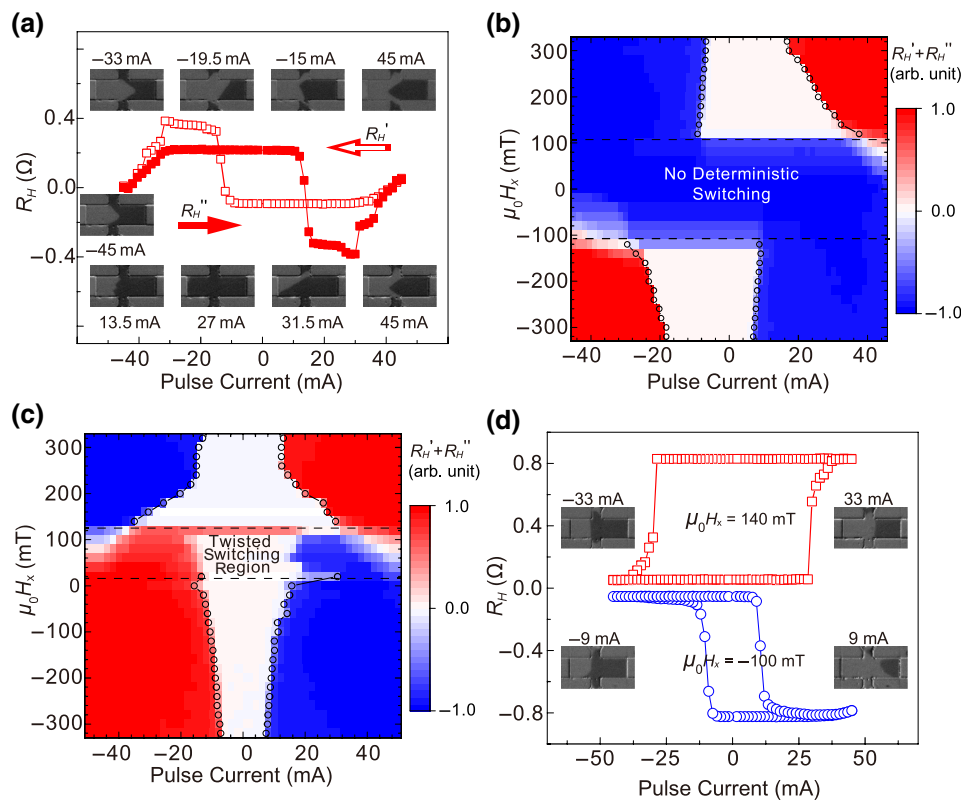


FIG. 4. Switching phase diagrams. (a) The twisted current-driven loop measured at $\mu_0 H_x = 80$ mT, State I. The MOKE images at the top (bottom) correspond to the descending (ascending) current amplitudes indicated by open (solid) squares. These two half pieces of a current-driven loop are defined as R_H' and R_H'' . (b) SPD of the central cross measured after a single setting field of $\mu_0 H_z = 600$ mT. The contrast of the SPD is based on the normalized sum of R_H' and R_H'' as defined in Fig. 3(c). The blue and red colors mean that the magnetization is only dominated by the last current pulse, regardless of the current-driven course. For monotonous deterministic switching, the critical currents are labeled by open circles. (c) SPD measured at State I. (d) Current-driven switching measured at $\mu_0 H_x = 140$ mT and $\mu_0 H_x = -100$ mT, State I. MOKE images indicate the DW profile during the switching process. Loops are staggered along the z axis.

twisted current-driven loop measured at $\mu_0 H_x = 80$ mT, State I, as shown in Fig. 4(a) (see Note 4 within the Supplementary Material) [35,44]. Referring to the opposite χ polarities of the State I curve and “Reference” curve at $\mu_0 H_x = 80$ mT shown in Fig. 3(b), the switching with low (high) I_{cri} belongs to the DW motion mode (nucleation-expansion mode). An intuitive way to compare these two modes is by magnetizing both pads with $\mu_0 H_x = 600$ mT. In this configuration, only the switching toward “down” magnetization can be assisted by the DW, while the switching toward “up” magnetization has to be done via the nucleation-expansion mode, similar to the first loop shown in Fig. 1(d). As shown in Fig. 4(b), the nucleation-expansion mode has larger I_{cri} values within the entire $\mu_0 H_x$ range, but shows stronger dependence on the $\mu_0 H_x$ value, regardless of the saturation of χ when $|\mu_0 H_x| > 200$ mT. The stronger response to $\mu_0 H_x$ implies that the nucleation-expansion mode relies on the in-plane field not only for chirality-breaking, but also for lowering the nucleation barrier. This asymmetric feature of the switching phase diagram (SPD) is similar to the results in our previous work on an antiferromagnetically coupled system, which shows good self-consistency of this device design [29].

Knowing the different features of two switching modes, the odd SPD of State I shown in Fig. 4(c) can be interpreted. In the field range $\mu_0 H_x \leq 0$ mT, the switching is totally dominated by the DW motion mode and I_{cri} decreases smoothly along with $\mu_0 H_x$, since the external field helps in stabilizing the chirality. As $0 \text{ mT} < \mu_0 H_x < 140$ mT, the I_{cri} of the nucleation-expansion mode is roughly indicated by the white valley between the blue and red areas occurring at the boundary of the diagram. In this region, the I_{cri} value of DW motion mode (nucleation-expansion mode) decreases (increases) with $\mu_0 H_x$, identical to the changes of χ values. After $\mu_0 H_x$ overrides the $\mu_0 H_{\text{DM}}$, the twisting of the switching loop disappears, indicating that the two switching modes share the same polarity again. Notably within the $\mu_0 H_x$ range of 150 to 240 mT, I_{cri} is following the trend of the nucleation-expansion mode. For $\mu_0 H_x > 240$ mT, I_{cri} keeps nearly constant. This implies that the switching in this region is a mixture of the two modes. The SPD of the DW-assisted device shows good consistency with the evolution of SOT efficiency.

E. Discussion: pinning effect in the DW motion switching

In the measurements of SOT efficiency and SPD, the pinning effect plays a minor role but results in interesting phenomena. The current-biased loops shown in Fig. 3(a) have obvious asymmetric shapes, and the sides that are nearer to the y axis show more skewed profile. This asymmetry corresponds to different DW profiles, as shown in

Fig. 3(a). The skewed side of the loop corresponds to the curved DW, similar to the ones occurring in the field-free switching discussed in section B, while the steeper side corresponds to the straight DW, nearly perpendicular to the edges of the Hall bar.

The pinning effect of the DW changes the competition between the SOT and the external field. At the initial stage of DW motion, the DW locates at the boundary of the Tb/Co multilayers as a relatively ideal straight line. At this stage, the \mathbf{m}_{DW} is along the x direction, ensuring a maximum SOT-driving force. When the DW starts to move, the pinning centers result in a bended profile of the DW. The bended sections of the DW in turn receive less SOT-driving force since the projection of \mathbf{m}_{DW} along the x direction decreases. In the switching event where SOT cooperates with the external field $\mu_0 H_z$, this decreasing trend of SOT after departure from the initial position prolongs the reversal time, resulting in a skewed profile. But for the other switching event in the same loop, the SOT competes with $\mu_0 H_z$, and the bending of the DW means an increase in the total driving force of the DW, which results in an avalanchelike propagation of the DW. Meanwhile, this negative feedback balances out the need for a larger driving force for depinning, keeping the DW straight. In the SPD measurement, the alignment of \mathbf{m}_{DW} by $\mu_0 H_x$ plays a similar role to $\mu_0 H_z$, as shown in the loops of Fig. 4(d). Under State I, $\mu_0 H_x$ of +140 mT competes with $\mu_0 H_{\text{DM}}$ on the aligning of \mathbf{m}_{DW} , building the negative feedback to the pinning effect and resulting in a straight DW. On the other hand, $\mu_0 H_x$ of -100 mT only supplies additional alignment of \mathbf{m}_{DW} along the x direction; hence, the DW remains the bended profile with smaller curvature similar to the field-free condition.

This hypothesis can also be used to explain the kinks at zero field in the $|\chi|-\mu_0 H_x$ curves. The $|\chi|$ values at $\mu_0 H_x = 0$ mT are around 80% of the saturating $|\chi|$ value and the slope differs at two sides, resulting in the kinks. This discontinuity means that the DMI-induced alignment of \mathbf{m}_{DW} suffers from tilting, while $\mu_0 H_x$ can uniformly align \mathbf{m}_{DW} regardless of the specific DW profile. This difference results in different slopes on each side of $\mu_0 H_x = 0$ mT. Meanwhile, if the DW is simplified into Néel-type sections, which are pinned at both ends, each section can be ideally bent into a semicircle before depinning [45], and the ratio of the total SOT-driving force of the entire DW to the χ value of a straight Néel-type DW is estimated to be 78.5%, i.e., the area ratio between a circle and its circumscribing square (see Note 3 within the Supplementary Material) [35]. This value is very close to the 80% mentioned previously, indicating a good accordance of this explanation. Since the tilting of a DW universally occurs in a racetrack device and is most of the time undesirable, for the device design with both effective in-plane field and DW racetrack [18], this mechanism could be applied to modify the profile of the DW. For DW-based

spin-Hall nano-oscillators which involve SOT, DW, and external field at the same time [46], this knowledge can be used to modify the performance of the oscillator.

F. SAF structure for potential MTJ application

To fulfill the potential of our device design as the free layer of a MTJ, a new FM layer is added above the Ru/Pt capping layer to form a SAF structure, otherwise the direct contact between the FM layer and the MgO tunneling layer will be impossible. A new stack is fabricated with additional deposition of Co(0.4–1.3 nm)/Pt(1 nm) between steps 3 and step 4 in Fig. 1(a). The Pt capping layer is added to prevent oxidation and to increase the PMA, whereas in the MTJ fabrication this layer can be replaced by a MgO tunneling layer. The R_H - H_z loops measured for the device with Co thickness $t_{\text{Co}} = 0.75$ nm show an antiferromagnetic curve with an additional switching between two SAF states, as indicated in Fig. 5(a) [47]. The States I and II defined above are also used for this device and the R_H - I_p loops are shown in Fig. 5(b). The difference between the two R_H levels corresponds to the two SAF states shown in Fig. 5(a), indicating that the DWs lead to the deterministic switching of the SAF structure. By varying the Co layer thickness, the net magnetization

can be largely decreased (see Note 5 within the Supplemental Material) [35]. The feasibility of driving the SAF magnetization by current allows the design of a field-free MTJ as illustrated in Fig. 5(d). As an additional benefit, each magnetic component in this design is either SAF or ferrimagnetic multilayers, which induce less disturbance by the stray field between devices in a highly integrated circuit [48].

Finally, we employ micromagnetic modeling to simulate the free-layer design shown in Fig. 5(c) [49]. In the top FM pillar of the model with diameter of 100 nm and thickness of 1 nm, the magnetic parameters including M_s , out-of-plane anisotropy K_u , SAF coupling strength J_{ex} and effective spin-Hall angle ξ_{SH} , come from the experimental data, except for the exchange constant J of $6 \times 10^{11} \text{ J m}^{-2}$. A field of 1 T is applied to two ends of the current channel to replace the role of the Tb/Co pads. When a direct current of $6 \times 10^{11} \text{ A m}^{-2}$ is injected into the current channel, the set DW moves toward the pillar and brings the multidomain structure into the pillar. The sweeping of coupled DWs achieves magnetization reversal in the pillar. The strong pinning effect locates on the edge of the pillar where the coupling condition changes drastically. After 300 ps, the DW stops at the boundary of the region with the

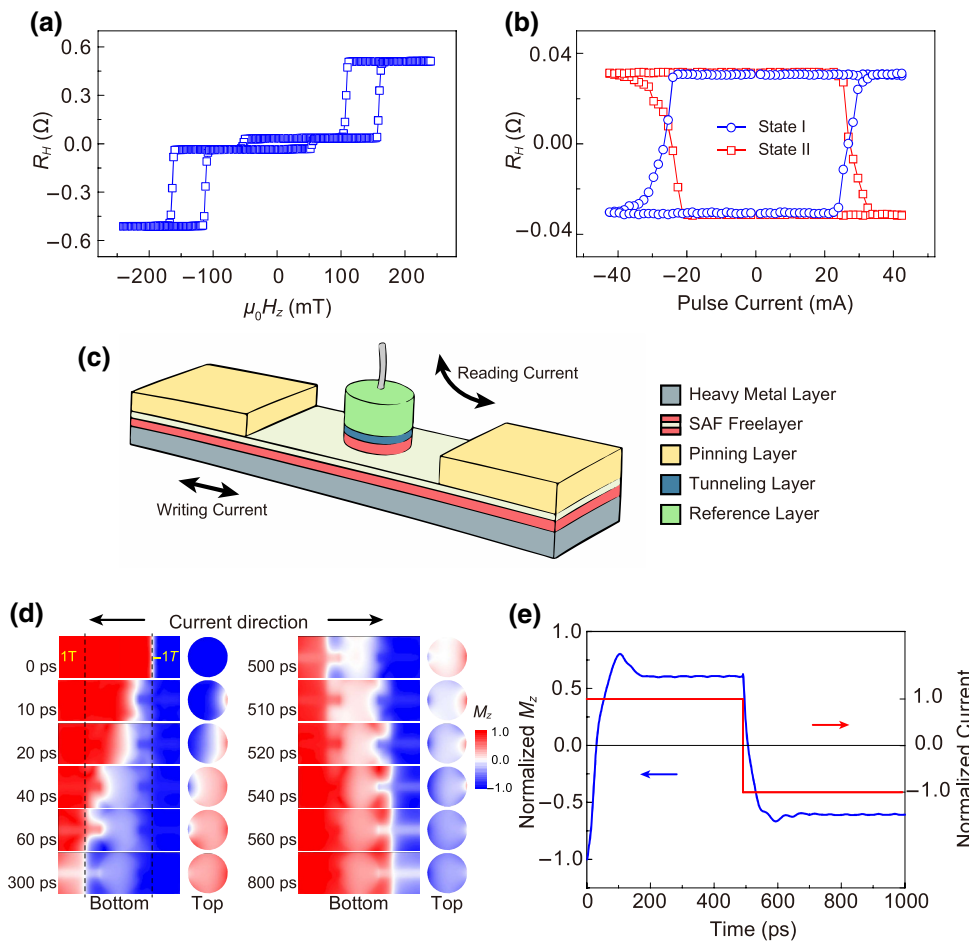


FIG. 5. SAF structure device design. (a) R_H vs H_z loop and (b) R_H vs I_p loops in State I and II of a SAF device with $t_{\text{Co}} = 0.75$ nm. (c) Schematic illustration of the MRAM design utilizing the DW motion SAF structure. (d) The evolving M_z distribution of the micromagnetic model during DW-assisted current-driven switching. (e) The change of total M_z in the pillar (blue) and current in the bottom layer (red) during simulation.

pinning field. The DWs show similar behavior when the polarity of the current is changed, reversing the magnetization in the pillar back to downward, as shown in Fig. 5(d). The total magnetization of the pillar shown in Fig. 5(e) indicates that the reversal process can be done in 200 ps, which compares competitively to semiconductor memories [50]. Notably, the magnetization is not reversed to saturation value because of the small current density, while larger current density can achieve total reversal but results in dissipation of the DWs. The simulation results indicate that this design is feasible, although the shape should be modified to minimize the undesirable pinning effect.

IV. CONCLUSION

In conclusion, we propose a field-free current-driven magnetization-switching device with additional Tb/Co multilayers for DW creation. The switching of the magnetization is proven by MOKE imaging to be dominated by the motion of the DW created at the boundary of the coupled areas. We measure the SOT efficiency of DW motion switching mode, which is determined by the orientation of the in-plane spins in the assisting DWs. The competition between the two switching modes forms an asymmetric SPD, which can be qualitatively explained by the amplitude of SOT efficiency. Under the influence of the pinning effect, the competition between uniform external field and DMI on DW magnetization results in avalanche-like switching and a straight DW profile. Finally, SAF structure in the central area of the device is investigated by experiment and micromagnetic simulation to prove that this design can be used in the manufacture of MTJ-based memory.

ACKNOWLEDGMENTS

We thank Wei He, Hongxin Yang, and Zheng Han for discussions. This work has been supported by the State Key Project of Research and Development of China (No. 2017YFA0206302), and the National Nature Science Foundation of China under projects No. 51590883, No. 51771198, and No. 51801212.

-
- [1] I. Mihai Miron, K. Garello, G. Gaudin, P.-J. Zermatten, M. V. Costache, S. Auffret, S. Bandiera, B. Rodmacq, A. Schuhl, and P. Gambardella, Perpendicular switching of a single ferromagnetic layer induced by in-plane current injection, *Nature* **476**, 189 (2011).
 - [2] L. Liu, O. J. Lee, T. J. Gudmundsen, D. C. Ralph, and R. A. Buhrman, Current-Induced Switching of Perpendicularly Magnetized Magnetic Layers Using Spin Torque From the Spin Hall Effect, *Phys. Rev. Lett.* **109**, 096602 (2012).
 - [3] L. J. Zhu, D. C. Ralph, and R. A. Buhrman, Highly Efficient Spin-Current Generation by the Spin Hall Effect in Au_{1-x}Ptx, *Phys. Rev. Appl.* **10**, 031001 (2018).

- [4] N. H. D. Khang, Y. Ueda, and P. N. Hai, A conductive topological insulator with large spin hall effect for ultralow power spin-orbit torque switching, *Nat. Mater.* **17**, 808 (2018).
- [5] L. Zhu, K. Sobotkiewich, X. Ma, X. Li, D. C. Ralph, and R. A. Buhrman, Strong damping-like spin-orbit torque and tunable dzyaloshinskii-moriya interaction generated by Low-resistivity Pd_{1-x}Ptx alloys, *Adv. Funct. Mater.* **29**, 1805822 (2019).
- [6] L. J. Zhu, D. C. Ralph, and R. A. Buhrman, Spin-Orbit Torques in Heavy-Metal-Ferromagnet Bilayers with Varying Strengths of Interfacial Spin-Orbit Coupling, *Phys. Rev. Lett.* **122**, 077201 (2019).
- [7] C.-F. Pai, Y. Ou, L. H. Vilela-Leão, D. C. Ralph, and R. A. Buhrman, Dependence of the efficiency of spin hall torque on the transparency of Pt/ferromagnetic layer interfaces, *Phys. Rev. B* **92**, 064426 (2015).
- [8] X. Qiu, W. Legrand, P. He, Y. Wu, J. Yu, R. Ramaswamy, A. Manchon, and H. Yang, Enhanced Spin-Orbit Torque via Modulation of Spin Current Absorption, *Phys. Rev. Lett.* **117**, 217206 (2016).
- [9] S. K. Li, X. T. Zhao, W. Liu, Y. H. Song, L. Liu, X. G. Zhao, and Z. D. Zhang, Interface effect of ultrathin Wlayer on spin-orbit torque in Ta/W/CoFeB multilayers, *Appl. Phys. Lett.* **114**, 082402 (2019).
- [10] S. K. Li, X. T. Zhao, W. Liu, T. T. Wang, X. G. Zhao, and Z. D. Zhang, Enhanced spin-orbit torques and perpendicular magnetic anisotropy in CoFeB/MgO structures with Ta/W bilayer, *AIP Adv.* **8**, 065007 (2018).
- [11] P. P. J. Haazen, E. Mure, J. H. Franken, R. Lavrijsen, H. J. M. Swagten, and B. Koopmans, Domain wall depinning governed by the spin hall effect, *Nat. Mater.* **12**, 299 (2013).
- [12] O. J. Lee, L. Q. Liu, C. F. Pai, Y. Li, H. W. Tseng, P. G. Gowtham, J. P. Park, D. C. Ralph, and R. A. Buhrman, Central role of domain wall depinning for perpendicular magnetization switching driven by spin torque from the spin hall effect, *Phys. Rev. B* **89**, 024418 (2014).
- [13] S. Fukami, C. Zhang, S. DuttaGupta, A. Kurenkov, and H. Ohno, Magnetization switching by spin-orbit torque in an antiferromagnet-ferromagnet bilayer system, *Nat. Mater.* **15**, 535 (2016).
- [14] S. A. Razavi, D. Wu, G. Yu, Y.-C. Lau, K. L. Wong, W. Zhu, C. He, Z. Zhang, J. M. D. Coey, P. Stamenov, P. K. Amiri, and K. L. Wang, Joule Heating Effect on Field-Free Magnetization Switching by Spin-Orbit Torque in Exchange-Biased Systems, *Phys. Rev. Appl.* **7**, 024023 (2017).
- [15] Y.-W. Oh, S.-H. C. Baek, Y. M. Kim, H. Y. Lee, K.-D. Lee, C.-G. Yang, E.-S. Park, K.-S. Lee, K.-W. Kim, G. Go, J.-R. Jeong, B.-C. Min, H.-W. Lee, K.-J. Lee, and B.-G. Park, Field-free switching of perpendicular magnetization through spin-orbit torque in antiferromagnet/ferromagnet/oxide structures, *Nat. Nanotechnol.* **11**, 878 (2016).
- [16] Y. C. Lau, D. Betto, K. Rode, J. M. D. Coey, and P. Stamenov, Spin-orbit torque switching without an external field using interlayer exchange coupling, *Nat. Nanotechnol.* **11**, 758 (2016).
- [17] Y. Liu, B. Zhou, and J.-G. Zhu, Field-free magnetization switching by utilizing the spin hall effect and interlayer exchange coupling of iridium, *Sci. Rep.* **9**, 325 (2019).

- [18] N. Murray, W.-B. Liao, T.-C. Wang, L.-J. Chang, L.-Z. Tsai, T.-Y. Tsai, S.-F. Lee, and C.-F. Pai, Field-free spin-orbit torque switching through domain wall motion, *Phys. Rev. B* **100**, 104441 (2019).
- [19] G. Yu, P. Upadhyaya, Y. Fan, J. G. Alzate, W. Jiang, K. L. Wong, S. Takei, S. A. Bender, L.-T. Chang, Y. Jiang, M. Lang, J. Tang, Y. Wang, Y. Tserkovnyak, P. K. Amiri, and K. L. Wang, Switching of perpendicular magnetization by spin-orbit torques in the absence of external magnetic fields, *Nat. Nanotechnol.* **9**, 548 (2014).
- [20] T.-Y. Chen, H.-I. Chan, W.-B. Liao, and C.-F. Pai, Current-Induced Spin-Orbit Torque and Field-Free Switching in Mo-Based Magnetic Heterostructures, *Phys. Rev. Appl.* **10**, 044038 (2018).
- [21] K. Cai, M. Yang, H. Ju, S. Wang, Y. Ji, B. Li, K. W. Edmonds, Y. Sheng, B. Zhang, N. Zhang, S. Liu, H. Zheng, and K. Wang, Electric field control of deterministic current-induced magnetization switching in a hybrid ferromagnetic/ferroelectric structure, *Nat. Mater.* **16**, 712 (2017).
- [22] M. Wang, W. Cai, D. Zhu, Z. Wang, J. Kan, Z. Zhao, K. Cao, Z. Wang, Y. Zhang, T. Zhang, C. Park, J.-P. Wang, A. Fert, and W. Zhao, Field-free switching of a perpendicular magnetic tunnel junction through the interplay of spin-orbit and spin-transfer torques, *Nat. Electron.* **1**, 582 (2018).
- [23] G. Yu, P. Upadhyaya, Q. Shao, H. Wu, G. Yin, X. Li, C. He, W. Jiang, X. Han, P. K. Amiri, and K. L. Wang, Room-Temperature skyrmion shift device for memory application, *Nano Lett.* **17**, 261 (2017).
- [24] K.-S. Ryu, S.-H. Yang, L. Thomas, and S. S. P. Parkin, Chiral spin torque arising from proximity-induced magnetization, *Nat. Commun.* **5**, 3910 (2014).
- [25] S. A. Siddiqui, J. Han, J. T. Finley, C. A. Ross, and L. Liu, Current-Induced Domain Wall Motion in a Compensated Ferrimagnet, *Phys. Rev. Lett.* **121**, 057701 (2018).
- [26] H. Honjo, S. Fukami, T. Suzuki, R. Nebashi, N. Ishiwata, S. Miura, N. Sakimura, T. Sugibayashi, N. Kasai, and H. Ohno, Domain-wall-motion cell with perpendicular anisotropy wire and in-plane magnetic tunneling junctions, *J. Appl. Phys.* **111**, 07c903 (2012).
- [27] J. M. Lee, K. Cai, G. Yang, Y. Liu, R. Ramaswamy, P. He, and H. Yang, Field-Free spin-orbit torque switching from geometrical domain-wall pinning, *Nano Lett.* **18**, 4669 (2018).
- [28] B. Cui, D. Li, J. Yun, Y. Zuo, X. Guo, K. Wu, X. Zhang, Y. Wang, L. Xi, and D. Xue, Magnetization switching through domain wall motion in Pt/Co/Cr racetracks with the assistance of the accompanying joule heating effect, *Phys. Chem. Chem. Phys.* **20**, 9904 (2018).
- [29] X. Zhao, W. Liu, S. Li, T. Wang, L. Liu, Y. Song, S. Ma, X. Zhao, and Z. Zhang, Asymmetric current-driven switching of synthetic antiferromagnets with Pt insert layers, *Nanoscale* **10**, 7612 (2018).
- [30] J. Torrejon, J. Kim, J. Sinha, S. Mitani, M. Hayashi, M. Yamanouchi, and H. Ohno, Interface control of the magnetic chirality in CoFeB/MgO heterostructures with heavy-metal underlayers, *Nat. Commun.* **5**, 5655 (2014).
- [31] S. S. P. Parkin, N. More, and K. P. Roche, Oscillations in Exchange Coupling and Magnetoresistance in Metallic Superlattice Structures - Co/Ru, Co/Cr, and Fe/Cr, *Phys. Rev. Lett.* **64**, 2304 (1990).
- [32] S. Bandiera, R. C. Sousa, S. Auffret, B. Rodmacq, and B. Dieny, Enhancement of perpendicular magnetic anisotropy thanks to Pt insertions in synthetic antiferromagnets, *Appl. Phys. Lett.* **101**, 072410 (2012).
- [33] X. T. Zhao, Y. Q. Zhao, W. Liu, Z. M. Dai, T. T. Wang, X. G. Zhao, and Z. D. Zhang, Magnetization reversal of antiferromagnetically coupled perpendicular anisotropy films driven by current, *J. Mater. Sci. Technol.* **34**, 832 (2018).
- [34] C.-F. Pai, M. Mann, A. J. Tan, and G. S. D. Beach, Determination of spin torque efficiencies in heterostructures with perpendicular magnetic anisotropy, *Phys. Rev. B* **93**, 144409 (2016).
- [35] See Supplemental Material at <http://link.aps.org/supplemental/10.1103/PhysRevApplied.13.044074> for the RKKY coupling between a 3d ferromagnetic layer and a 3d-4f multilayer, measurement of the effective field generated by spin-orbit torque using a harmonic method, the influence of domain wall (DW) pinning, the partial switching behavior, the deterministic switching of the synthetic antiferromagnet, and SPD measured under State II.
- [36] M. D. Stiles, Interlayer exchange coupling, *J. Magn. Magn. Mater.* **200**, 322 (1999).
- [37] S.-H. Yang, K.-S. Ryu, and S. Parkin, Domain-wall velocities of up to 750 m s⁻¹ driven by exchange-coupling torque in synthetic antiferromagnets, *Nat. Nanotechnol.* **10**, 221 (2015).
- [38] T. C. Wang, T. Y. Chen, H. W. Yen, and C. F. Pai, Comparative study on spin-orbit torque efficiencies from W/ferromagnetic and W/ferrimagnetic heterostructures, *Phys. Rev. Mater.* **2**, 014403 (2018).
- [39] D. Khadka, S. Karayev, and S. X. Huang, Dzyaloshinskii-Moriya interaction in Pt/Co/Ir and Pt/Co/Ru multilayer films, *J. Appl. Phys.* **123**, 123905 (2018).
- [40] A. V. Khvalkovskiy, V. Cros, D. Apalkov, V. Nikitin, M. Krounbi, K. A. Zvezdin, A. Anane, J. Grollier, and A. Fert, Matching domain-wall configuration and spin-orbit torques for efficient domain-wall motion, *Phys. Rev. B* **87**, 020402 (2013).
- [41] M. Hayashi, J. Kim, M. Yamanouchi, and H. Ohno, Quantitative characterization of the spin-orbit torque using harmonic hall voltage measurements, *Phys. Rev. B* **89**, 144425 (2014).
- [42] S. Woo, M. Mann, A. J. Tan, L. Caretta, and G. S. D. Beach, Enhanced spin-orbit torques in Pt/Co/Ta heterostructures, *Appl. Phys. Lett.* **105**, 212404 (2014).
- [43] A. Thiaville, S. Rohart, E. Jue, V. Cros, and A. Fert, Dynamics of dzyaloshinskii domain walls in ultrathin magnetic films, *Europhys. Lett.* **100**, 57002 (2012).
- [44] J. Yu, X. Qiu, Y. Wu, J. Yoon, P. Deorani, J. M. Besbas, A. Manchon, and H. Yang, Spin orbit torques and dzyaloshinskii-moriya interaction in dual-interfaced Co-Ni multilayers, *Sci. Rep.* **6**, 32629 (2016).
- [45] X. Zhang, N. Vernier, W. Zhao, H. Yu, L. Vila, Y. Zhang, and D. Ravelosona, Direct Observation of Domain-Wall Surface Tension by Deflating or Inflating a Magnetic Bubble, *Phys. Rev. Appl.* **9**, 024032 (2018).
- [46] N. Sato, K. Schultheiss, L. Koerber, N. Puwenberg, T. Muehl, A. A. Awad, S. S. P. K. Arekapudi, O. Hellwig, J. Fassbender, and H. Schultheiss, Domain Wall Based

- Spin-Hall Nano-Oscillators, *Phys. Rev. Lett.* **123**, 057204 (2019).
- [47] O. Hellwig, A. Berger, J. B. Kortright, and E. E. Fullerton, Domain structure and magnetization reversal of antiferromagnetically coupled perpendicular anisotropy films, *J. Magn. Magn. Mater.* **319**, 13 (2007).
- [48] G. Y. Shi, C. H. Wan, Y. S. Chang, F. Li, X. J. Zhou, P. X. Zhang, J. W. Cai, X. F. Han, F. Pan, and C. Song, Spin-orbit torque in MgO/CoFeB/Ta/CoFeB/MgO symmetric structure with interlayer antiferromagnetic coupling, *Phys. Rev. B* **95**, 104435 (2017).
- [49] M. J. Donahue and D. G. Porter, OOMMF User's Guide, Version 1.0 (1999).
- [50] J. K. Kim, K. Sakui, S.-S. Lee, Y. Itoh, S.-C. Kwon, K. Kanazawa, K.-J. Lee, H. Nakamura, K.-Y. Kim, and T. Himeno, A 120-mm² 64-Mb NAND flash memory achieving 180 ns/byte effective program speed, *IEEE J. Solid-State Circuits* **32**, 670 (1997).

Correction: The previously published Figure 2 contained errors in the direction of some of the arrows and has been replaced.